Numerical analysis with joint model on RC assemblages subjected to progressive collapse

Tan, Kang Hai; Yu, Jun

2014

Tan, K. H., & Yu, J. (2014). Numerical analysis with joint model on RC assemblages subjected to progressive collapse. Magazine of concrete research, 66(23), 1201-1218.

https://hdl.handle.net/10356/103372

https://doi.org/10.1680/macr.14.00100

Magazine of Concrete Research
Volume 66 Issue 23

Numerical analysis with joint model on RC assemblages subjected to progressive collapse
Yu and Tan

Magazine of Concrete Research, 2014, **66**(23), 1201–1218
http://dx.doi.org/10.1680/macr.14.00100
Paper 1400100
Received 04/04/2014; revised 18/05/2014; accepted 20/05/2014
Published online ahead of print 11/07/2014

ice
Institution of Civil Engineers
publishing

Numerical analysis with joint model on RC assemblages subjected to progressive collapse

Jun Yu
Associate Professor, College of Civil and Transportation Engineering, Hohai University, Nanjing, China

Kang Hai Tan
Professor, School of Civil & Environmental Engineering, Nanyang Technological University, Singapore

The behaviour of structures subjected to progressive collapse is typically investigated by introducing column-removing scenarios. Previous experimental results show that large-deformation performances of reinforced concrete (RC) assemblages under a middle column removal scenario (MCRS) involve discontinuity due to bar slip and fracture near the joint interfaces. To consider the effects of the discontinuity on structural behaviour, a component-based joint model is introduced into macromodel-based finite-element analysis (macro-FEA), in which beams are modelled as fibre elements. The joint model consists of a series of non-linear springs, each of which represents a load transfer path from adjoining members to a joint. The calibration procedures of spring properties are illustrated systematically. In particular, a macro-bar stress–slip model is developed to consider the effects of large post-yield tensile strains and finite embedment lengths on the bar stress–slip relationship. Comparisons of simulated and observed responses for a series of RC assemblages indicate that macro-FEA incorporating the joint model is a practical approach to simulate the essential structural behaviour of RC assemblages under a MCRS, including catenary action. Finally, the macro numerical model is used to investigate the effects of boundary conditions, bar curtailment and beam depth on the structural behaviour of RC assemblages. The results suggest that beam depth affects the fixed-end rotation contributed by bar slip, and further significantly influences the development of catenary action.

Notation

A_b	bar cross-sectional area
A'_s	compressive bar area
a'_s	distance from extreme compression concrete fibre to centroid of compression reinforcement at joint interfaces
b	width of beam
C_c	compressive force contributed by concrete
C_s	compressive force contributed by steel reinforcement
c_N	neutral-axis depth of beam
d_b	bar diameter
d_j	depth of joint panel
E_h	hardening modulus of reinforcing bars
E_s	elastic modulus of reinforcing bars
F_{mt}	force equal to $(F_{yt} + F_{ut})/2$
F_s	forces in two diagonal springs representing shear panel behaviour
F_{ut}	force of springs k_{bb} and k_{bt} corresponding to the smaller capacity based on bar fracture or pullout
F_{yt}	force of springs k_{bb} and k_{bt} corresponding to the bar yielding in tension
f'_c	compressive strength of concrete
f_s	applied axial stress at loaded end of bar
f_{se}	maximum elastic bar stress applied in the available elastic length l_e under pulling force
f_u	ultimate tensile strength of reinforcing bars
f_y	yield strength of reinforcing bars
f'_y	artificial yield strength to make bilinear constitutive models of reinforcement have the same strain energy as that from material tests up to bar fracture
K_a	equivalent axial restraint stiffness at two-bay beam ends
K_r	equivalent rotational restraint stiffness at two-bay beam ends
k_{bb}	bar force–slip springs along the centroid of the top reinforcement layers at a joint interface
k_{bs}	interface spring at a joint interface
k_{bt}	bar force–slip springs along the centroid of the bottom reinforcement layers at a joint interface
k_s	joint panel spring representing shear panel behaviour
l_e	available elastic length $(= l_{embd} - l_{yrq})$
l_{ed}	elastic development length for reducing yield strength to zero $(l_{ed} \geqslant l_{erq})$
l_{embd}	bar embedement length
l_{erq}	required elastic length for reducing maximum elastic stress to zero

l_j	diagonal length of joint panel
l_s	straight embedment length of anchored bars with hooks
l_{yrq}	required inelastic length for reducing maximum inelastic stress to yield strength
N_b	axial compression of beams corresponding to extreme compression concrete fibre reaching the ultimate strain simultaneously with tension reinforcement attaining the yield strain
N_u	maximum axial compression of beams
s	slip of bars at the joint interface (i.e. deformation of bar force–slip springs)
s_0	slip at unloaded end of reinforcing bar
s_1	slip corresponding to ultimate bond stress in the local bond–slip model proposed by Eligehausen *et al.* (1983)
s_{ext}	bar extension from zero stress point to a joint interface
T	axial tension of tensile reinforcing bars
β	ratio of equivalent rectangular stress block depth to neutral-axis depth
γ	shear distortion of joint panel
Δ	elongation and contraction of diagonal springs in joint panel
ε_{cu}	ultimate compressive strain of concrete
ε_{end}	strain at centre of a continuous bar
ε_h	hardening strain of reinforcing bars
ε_s	strain at loaded end of a bar
ε'_{scr}	strain of compression bars corresponding to concrete attaining ultimate compressive strain
ε_u	strain corresponding to ultimate tensile strength of reinforcing bars
ε_y	yield strain of reinforcing bars
θ	angle of diagonal line of a joint panel with respect to the horizontal
τ_e	elastic bond stress at the free end of a bar with inadequate embedment length
τ_{EC}	elastic compressive bond strength around a bar
τ_{ET}	elastic tensile bond strength around a bar
τ_p	shear stress along the perimeters of a joint panel
τ_u	ultimate bond stress in the local bond–slip model proposed by Eligehausen *et al.* (1983)
τ_{YC}	inelastic compressive bond strength around a bar
τ_{YT}	inelastic tensile bond strength around a bar

Introduction

With increasing threat of terrorist attacks, the progressive collapse of structures under extreme loading is a concern for government agencies. The alternate load path (ALP) approach recommended in design guidelines (DoD, 2010; GSA, 2003) requires checks on whether the remaining structure can bridge over missing columns. Furthermore, non-linear static analysis can be used to evaluate progressive collapse capacity by way of dynamic load amplification factors (DoD, 2010) or energy-based approaches (Dusenberry and Hamburger, 2006; Izzuddin *et al.*, 2008).

To find out the potential ALPs of reinforced concrete (RC) structures against progressive collapse, tests have been conducted on RC assemblages under a middle column removal scenario (MCRS) (Sadek *et al.*, 2011; Yi *et al.*, 2008; Yu and Tan, 2013a, 2013b). The experimental results show that with adequate lateral restraints, ALPs transit from a flexural mechanism at small deformations to catenary action at large deformations. Moreover, catenary action can provide larger structural resistance but is significantly affected by the rotation capacities and the failures of beam–column connections. For example, at the end of catenary action stage in the tests (Yu and Tan, 2013b), wide cracking and bar fracture occurred at or near the middle joint and end-column stub (ECS) interfaces, as shown in Figure 1(a). For the bars lap-spliced in the middle joint region, local failure occurred at the free ends of the lap-spliced bars, as shown in Figure 1(b). Those failures caused discontinuous zones in the development of catenary action. Therefore, it is necessary to extract the joints and to model them as independent elements when analysing structural behaviour at large deformations.

Over recent years, some numerical studies (Cesare and Archilla, 2006; Grierson *et al.*, 2005) have been dedicated to assessing global structural behaviour under progressive collapse by introducing simplified assumptions for modelling beams and columns, without considering the effects of joints. On the other hand, high-fidelity analyses (Hansen *et al.*, 2006; Luccioni *et al.*, 2004) were able to vividly demonstrate the failure process of structures subjected to abnormal loading, but were too computationally demanding and not practical for engineers. Recently, macromodel-based finite-element analysis (macro-FEA) has emerged as an effective approach to analyse structural behaviour under a MCRS, with considering the effects of joint failures (Bao *et al.*, 2008; Yu and Tan, 2013a). In macro-FEA, beams and columns are modelled with fibre elements, and joints with a series of springs, in so-called component-based joint models. However, there is a lack of careful calibration of the springs to consider the character of load transfer under a MCRS.

This paper attempts to make macro-FEA a practical and feasible approach for analysing the structural responses of RC structures under a MCRS. To this end, component-based joint models are modified and employed in macro-FEA using the software Engineer's Studio (Forum8, 2008) to conduct non-linear static analysis of RC assemblages. The validity of macro-FEA is evaluated by experimental results. The procedures to calibrate each component (or spring) in the joint model are provided, with special attention to the tensile bar force–slip spring, which governs bar fracture and the ensuing discontinuity in the structural response. Accordingly, a macro-bar stress–slip model is developed to consider the effects of large post-yield tensile strains and finite embedment lengths of bars on the bar stress–slip relationship. Finally, the validated numerical model is used to investigate the effects of boundary conditions, bar curtailment and beam depth on the structural behaviour of RC assemblages under a MCRS.

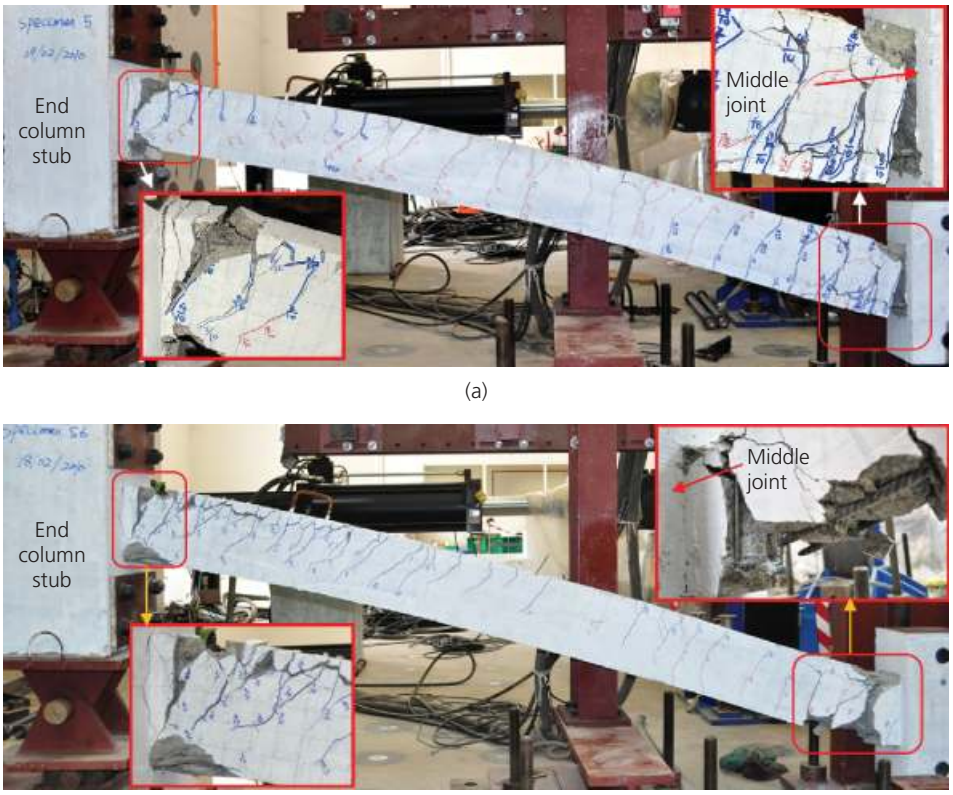

Figure 1. Failure modes of one-bay beam in RC assemblages: (a) with continuous bottom bars at the middle joint; (b) with lap-spliced bottom bars at the middle joint

Description of component-based joint model

The principle of the component-based joint model is to decompose the complex mechanisms of a joint into a series of simple components, each of which represents a unique load transfer path and can be characterised by an equivalent uniaxial non-linear spring (Jaspart, 2000). To consider the contribution of joint panel distortion and bar slip at joint interfaces to RC structure deformations, the idea of modelling RC joints as an assembly of springs has been employed in seismic research (Lowes and Altoontash, 2003; Mitra and Lowes, 2007; Youssef and Ghobarah, 2001) and, more recently, in progressive collapse (Bao *et al.*, 2008; Yu and Tan, 2013a).

Configurations of RC joints are regular, and load transfer paths from adjoining members to joints are limited. Therefore, the models proposed by Youssef and Ghobarah (2001) and Lowes and Altoontash (2003) are generic to cast in situ RC joints. Conceptually similar to these models, a joint model was modified to simulate structural behaviour under a MCRS, as shown in Figure 2. As no failure occurs at the connections of the column–joint interfaces, they are assumed rigid. The following three types of springs are used in this joint model.

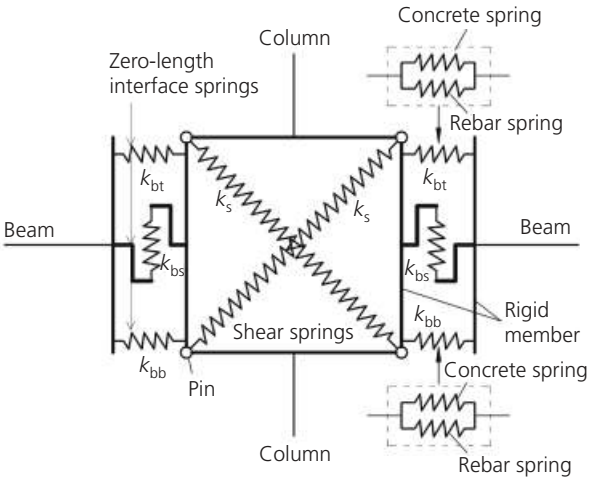

Figure 2. Proposed component-based joint model

- Joint panel spring (k_s). The joint panel is characterised by four pins and four rigid members enclosing the joint, as shown in Figure 2. Two diagonal springs represent the ability to resist shear distortion in the joint panel. Although shear

distortion is not appreciable for interior joints under a MCRS (Yu and Tan, 2013b), it could be dominant for exterior joints.

- Joint interface spring (k_{bs}). k_{bs} represents the shear transferred from the adjoining beams to the joint panel across the cracked joint interfaces. Conventional frame members have adequate shear capacity to preclude shear failure, and no interface shear failure is observed in the assemblage tests. Therefore, k_{bs} is taken as an elastic linear spring with a large stiffness as suggested by Lowes and Altoontash (2003).
- Bar force–slip springs (k_{bb} and k_{bt}). The pair of springs k_{bb} and k_{bt} represent the bending moment combined with the beam axial force transferred into the joint panel. Each spring should include the contribution from both concrete and reinforcement. However, the tensile contribution from concrete is typically ignored. In assemblage tests (Yu and Tan, 2013a, 2013b), it was found that flexural and axial action were most dominant, and the tests were eventually stopped due to the fracture of k_{bb} and k_{bt} at some joint interfaces. Therefore, the tensile bar force–slip relationship is the most critical in a MCRS.

The load transfer mechanisms of RC assemblages under a MCRS show that with increasing beam deflection, k_{bt} at the middle joint will transition from a compressive spring to a tensile spring, whereas k_{bb} always works as a tensile spring. Therefore, k_{bt} and k_{bb} are specified at the centroid of reinforcement at the joint interfaces in this paper. However, previous research either put k_{bt} and k_{bb} at the four corners of a joint panel (Lowes and Altoontash, 2003) or located them at the centroid of beam flexural compression and tension zones respectively (Mitra and Lowes, 2007; Youssef and Ghobarah, 2001).

In this paper, only calibration of the envelopes of the spring force–deformation relationships is considered. However, detailed information about unloading and reloading of the springs can be found in the help document of Engineer's Studio (Forum8, 2008).

Calibration of spring components in joint models

Shear panel spring

Based on the modified compression field theory (Vecchio and Collins, 1986), the relationship between shear stress τ_p in a joint panel and shear distortion γ can be obtained using the program Membrane 2000 (Bentz, 2000). Then the relationship τ_p–γ can be converted into the force–deformation relationship of two diagonal springs. The force in each diagonal spring F_s can be calculated through force equilibrium at a pin, as shown in Figure 3(a), from

$$1. \quad F_s = \tau_p d_j l_j / 2$$

where d_j and l_j are the joint depth and the diagonal length of the joint panel respectively.

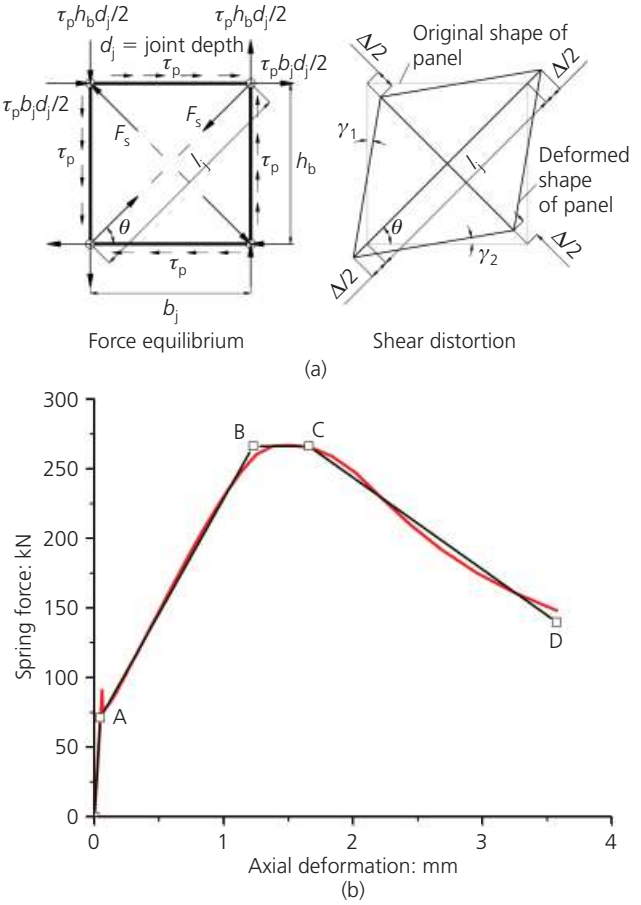

Figure 3. Shear panel spring k_s: (a) conversion of shear panel; (b) envelope of k_s (symmetric)

Since the stiffnesses of the two springs are equal due to symmetry, elongation of one spring equals contraction of the other. According to the geometric relationship shown in Figure 3(a), shear distortion is given by Youssef and Ghobarah (2001) as

$$2. \quad \gamma = 2\Delta / l_j \sin 2\theta$$

where θ is the angle of the diagonal line of the joint with respect to the horizontal direction.

Due to symmetry, only the positive branch of the shear panel spring is shown in Figure 3(b). The non-linear force–deformation relationship is then simplified into a multi-linear relationship. The critical points to determine the multi-linear model are located at the intersections of lines from linear regression at each segment (Table 1).

Tensile bar force–slip spring

Assuming uniform bond, stress in the elastic and plastic part of an anchored bar is efficient in determining the bar force–slip relationship at the loaded end (Alsiwat and Saatcioglu, 1992;

Critical point	Deformation: mm	Force: kN
A	0·046	71·17
B	1·230	266·13
C	1·660	266·13
D	3·570	139·87

Table 1. Properties of shear panels in RC sub-assemblages

Lowes and Altoontash, 2003). The model of Alsiwat and Saatcioglu assumes that the reinforcement constitutive model has no effect on inelastic bond strength, but Viawanthanatepa *et al.* (1979) pointed out that the selection of reinforcement constitutive models affects the evaluation of inelastic bond stress. The model of Lowes and Altoontash assumes that the embedment length is adequate so that zero-slip–stress conditions can be achieved at a point far away from the loaded end. However, these two models have a deficiency under a MCRS, in which large inelastic strains develop prior to bar fracture and zero-slip–stress conditions may not be satisfied due to the finite embedment lengths of bars extending from beams to joints. To consider the effects of high post-yield stress and finite embedment length, a simplified macro-bar stress–slip model is proposed with the following assumptions.

- Assumption 1: the distribution of bond stress within an elastic or inelastic part of a reinforcing bar remains uniform.
- Assumption 2: bar slip at the joint interfaces equals the bar extension over the embedment length plus the slip at the free end if any.
- Assumption 3: the constitutive model of the reinforcement is bilinear.

Reinforcing bars are typically continuous or lap-spliced in interior joints and anchored in exterior joints. Differences in the boundary conditions of continuous and anchored bars result in different strain and slip distributions over the embedment length and failure modes. Therefore, the two cases are introduced separately.

Slips of continuous bars at joint interfaces

Based on assumption 1, the distribution of bond stress τ and bar stress f of a continuous bar under applied axial tensile stress f_s at the interior joint interfaces is illustrated in Figure 4. Due to symmetry, one-half of the joint width is regarded as the bar embedment length l_{embd}. With constant inelastic bond strength τ_{YT}, the bar stress linearly decreases from f_s to the yield strength f_y over the inelastic length l_{yrq}. Similarly, with constant elastic bond strength τ_{ET}, the bar stress f is linearly distributed over the elastic length l_e. Even if the bar is stressed up to the centre, the associated slip is still zero due to symmetry. As a result, the slip s at each joint interface is solely determined by the bar extension s_{ext} according to assumption 2

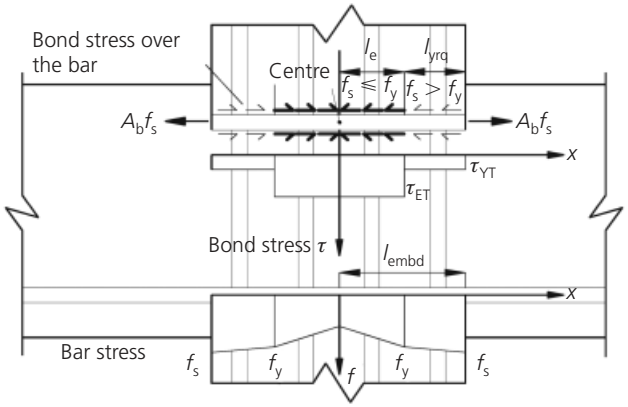

Figure 4. Bond and bar stress distribution of continuous bars under axial tension

$$s = s_{ext} = \int_0^l \varepsilon(x)\,dx \quad (3)$$

where $\varepsilon(x)$ is the strain at position x; $x = 0$ is defined at a point with zero-slip (for an interior joint with two equal-span beams at both sides, the point is the joint centre) and l is the smaller of the embedment length l_{embd} and the stressed length of the bar.

According to assumptions 1 and 3, it is derived that the bar strain is linearly distributed at the elastic and inelastic parts as well. Depending on the stress state and the embedment length l_{embd}, the strain profiles over l_{embd} can be divided into five categories, as shown in Figure 5. Due to symmetry, only one-half of the continuous bar is shown.

When the applied stress f_s is less than the yield strength f_y, as shown in Figures 5(a) and 5(b), the required elastic length l_{erq} can be determined from force equilibrium

$$f_s A_b = \tau_{ET} \pi d_b l_{erq} \quad (4)$$

where A_b is the nominal area of the bar and d_b is the bar diameter.

Therefore

$$l_{erq} = f_s d_b / 4\tau_{ET} \quad \text{when } f_s \leqslant f_y \quad (5)$$

When f_s attains f_y, l_{erq} becomes the elastic development length l_{ed} (i.e. $l_{ed} = f_y d_b / 4\tau_{ET}$). When f_s exceeds f_y, part of the bar is stressed inelastically with τ_{YT} mobilised over the required inelastic length l_{yrq}, and the strain profiles are shown in Figures 5(c) and 5(d). Therefore

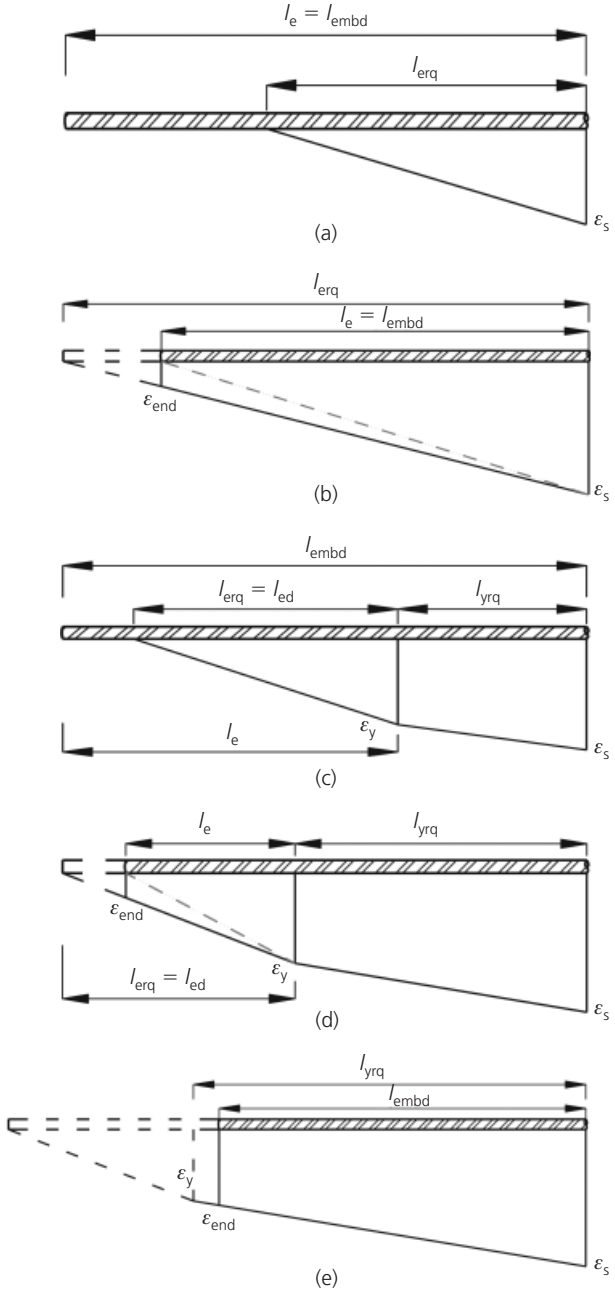

Figure 5. Categories of strain profiles under axial tension: (a) category 1, $f_s \leqslant f_y$ and $l_{erq} \leqslant l_{embd}$; (b) category 2, $f_s \leqslant f_y$ and $l_{erq} > l_{embd}$; (c) category 3, $f_s > f_y$ and $l_{ed} + l_{yrq} \leqslant l_{embd}$; (d) category 4, $f_s > f_y$ and $l_{ed} + l_{yrq} > l_{embd}$ but $l_{yrq} \leqslant l_{embd}$; (e) category 5, $f_s > f_y$ and $l_{yrq} > l_{embd}$

$$6. \quad f_s A_b = \tau_{YT} \pi d_b l_{yrq} + f_y A_b$$

Thus

$$7. \quad l_{yrq} = (f_s - f_y) d_b / 4\tau_{YT} \quad \text{when } f_s > f_y$$

Due to the finite dimensions of the joint, Figures 5(b) and 5(d) show that the available elastic length l_e, in which τ_{ET} is allowed to develop, is shorter than l_{erq}. Moreover, l_{yrq} may even exceed l_{embd}, as shown in Figure 5(e).

After the strain distribution over l_{embd} is determined, the slip due to bar extension is calculated using Equation 3. For example, the slip in category 4 shown in Figure 5(d) is calculated as

$$8. \quad s_{ext} = \frac{(\varepsilon_{end} + \varepsilon_y) l_e}{2} + \frac{(\varepsilon_y + \varepsilon_s) l_{yrq}}{2}$$

where l_{yrq} is given by Equation 7 and $l_e = l_{embd} - l_{yrq}$. Based on the bilinear constitutive model of reinforcement, the strain ε_s at the loaded end is

$$9. \quad \varepsilon_s = \varepsilon_y + \varepsilon_h = \frac{f_y}{E_s} + \frac{f_s - f_y}{E_h}$$

and ε_{end} at the centre of the continuous bar can be determined using a similar triangle

$$10. \quad \varepsilon_{end} = (l_{ed} - l_e)\varepsilon_y / l_{ed}$$

Substituting Equations 7, 9 and 10 into Equation 8 establishes the bar stress–slip relationship on the conditions that $f_s > f_y$ and $l_{ed} + l_{yrq} > l_{embd}$ but $l_{yrq} \leqslant l_{embd}$.

Slip of anchored bars at joint interfaces

If the embedment length l_{embd} of an anchored bar is adequate, the bar always exhibits a zero-slip–stress point, as shown in Figure 5(a) or 5(c). Otherwise, the bar can be stressed up to the free end (i.e. the physical cut-off point). In this case, the slip at the loaded end should include the bar extension s_{ext} and the free end slip s_0 (i.e. $s = s_{ext} + s_0$). Accordingly, the strain profile similar to the one shown in Figure 5(b) or 5(d) should be modified by the faint dashed lines to ensure zero-strain at the free end.

Compared with s_{ext}, s_0 is either zero or very small, but it is an indicator of pullout failure. Similar to the model presented by Alsiwat and Saatcioglu (1992), the local bond–slip model of Eligehausen *et al.* (1983) is used to obtain s_0

$$11. \quad s_0 = s_1 (\tau_e / \tau_u)^{2{\cdot}5}$$

where the ultimate bond stress τ_u and the corresponding slip s_1 are computed as

$$12. \quad \tau_u = (20 - d_b/4)(f'_c/30)^{0{\cdot}5}$$

13. $s_1 = (30/f'_c)^{0·5}$

where f'_c is concrete compressive strength (MPa) and τ_e in Equation 11 is the elastic bond stress at the free end of a bar, given by

14. $$\tau_e = \begin{cases} 0 & \text{if } l_e > l_{erq} \\ f_{se} d_b / 4 l_e & \text{if } l_e \leqslant l_{erq} \end{cases}$$

where f_{se} is the maximum elastic bar stress ($\leqslant f_y$) applied in the available elastic length l_e. For category 2 shown in Figure 5(b), $l_e = l_{embd}$, and for category 4 shown in Figure 5(d), $l_e = l_{embd} - l_{yrq}$. Equation 14 suggests that τ_e will be mobilised if l_e is shorter than the required elastic length l_{erq}. If τ_e reaches τ_u (i.e. $s_0 \geqslant s_1$), the bar will fail by pullout. Note that if $l_e = 0$, τ_e will become infinitely large. Therefore, an anchored bar can never develop the strain profile shown in Figure 5(e).

In practice, it is common to use hooks for anchorage of reinforcing bars in exterior RC joints. Filippou *et al.* (1983) suggested that a hooked bar can be modelled as a straight bar with an equivalent length of $l_{eq} = l_s + 5d_b$, where l_s is the straight embedment length. This recommendation is adopted in the proposed model.

Figure 6 shows the procedure to obtain tensile bar stress (force)–slip relationships. Note that it is unnecessary for a bar in the joint to go through each strain category shown in Figure 5 in a sequential manner. Following the above procedure, the bar force–slip relationship is characterised by a curve, which is then simplified into a multi-linear relationship. As shown in Figure 7, F_{yt} corresponds to the bar yielding in tension, F_{ut} denotes the smaller capacity based on bar fracture or pullout and $F_{mt} = (F_{yt} + F_{ut})/2$. The compressive branch of bar force–slip springs will be introduced later.

Determination of parameters of the macro-bar stress–slip model

The proposed macro-bar stress–slip model was verified by comparing the results with those predicted using a local bond–slip model (Yu and Tan, 2012). In implementing the macromodel, the elastic bond strength τ_{ET} is taken as $1·8(f'_c)^{0·5}$. Moreover, special attention should be given to the bar hardening modulus E_h and the inelastic bond strength τ_{YT}, as they significantly affect the ultimate slip. To capture bar fracture, E_h is calculated by equating the area enveloped by the original and the idealised bilinear bar stress–strain curves. This suggests that, at bar fracture, the bilinear model can absorb the same amount of strain energy as the original stress–strain relationship. To this end, an artificial yield strength f'_y is introduced, as indicated in Figure 8. Accordingly, E_h equals $E_h = (f_u - f'_y)/(\varepsilon_u - f'_y/E_s)$, where f_u and ε_u are the ultimate tensile strength and strain respectively. For typical reinforcement with f_u/f_y less than 1·25, f'_y approximately

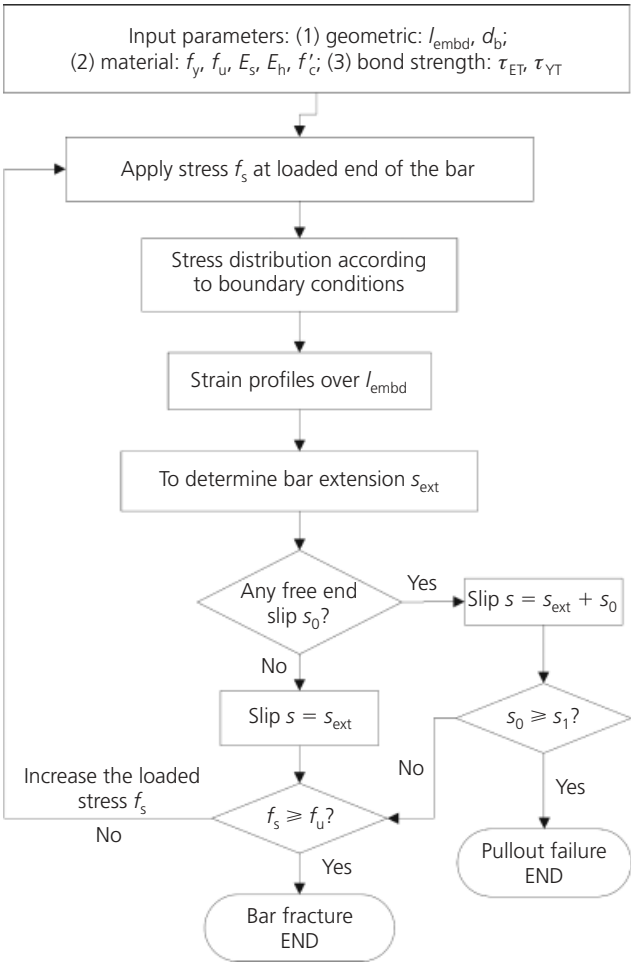

Figure 6. Procedure to determine tensile bar stress–slip relationship (f_u = ultimate tensile strength of bar)

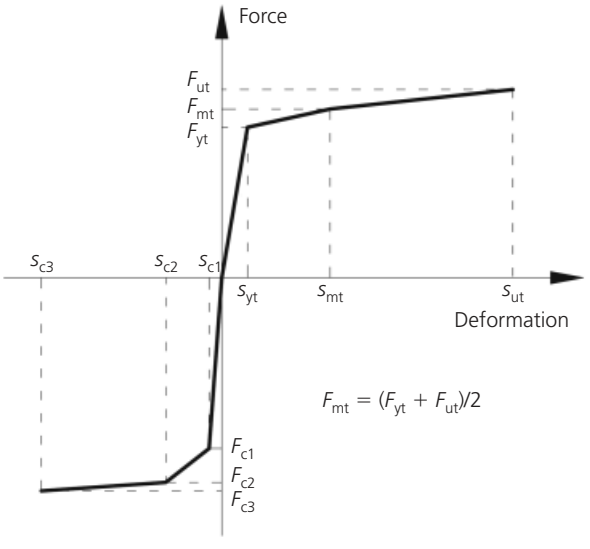

Figure 7. Bar force–slip for springs k_{bb} and k_{bt}

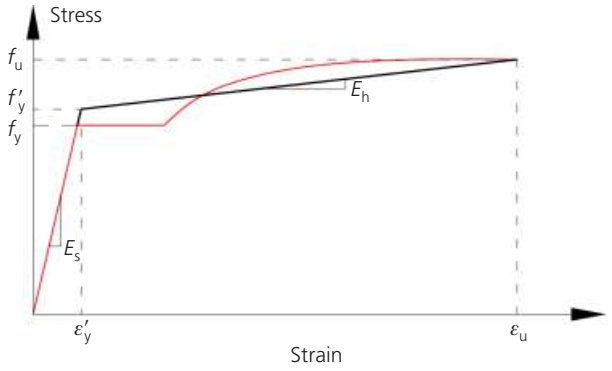

Figure 8. Constitutive model of steel reinforcement

equals f_y. With this bilinear model, τ_{YT} should be capped to $0{\cdot}3(f'_c)^{0{\cdot}5}$.

Compressive bar force–slip spring

As illustrated in Figure 2, the compressive force at the joint interfaces is made up of contributions from both the concrete (C_c) and the reinforcement (C_s). Both C_c and C_s are affected by the variation of the neutral-axis depth in the loading history. To determine the compressive bar force–slip relationship prior to structural analysis, the viable approach is to assume a constant neutral-axis depth and C_c linearly increasing with C_s (Lowes and Altoontash, 2003). However, the latter assumption overestimates C_c and makes the compressive spring extremely stiff, as concrete has limited compressive strength. Therefore, an alternative approach is needed.

At the joint interfaces of RC assemblages (Su *et al.*, 2009; Yu and Tan, 2013b), the ratio of N_u (the maximum axial compression) and N_b is 0·4–1·0; N_b is obtained from cross-sectional analysis at balanced failure, in which the extreme compression concrete fibre reaches the ultimate strain ε_{cu} (say, 0·003) simultaneously with tension reinforcement attaining the yield strain ε_y. Span-to-depth ratios of typical beams are in the range 8–12, becoming 16–24 in a MCRS. Within this range, N_u is smaller than $0{\cdot}7N_b$ (Yu, 2012). Therefore, the neutral-axis depth c_N corresponding to $N_u = 0{\cdot}7N_b$ allows typical beams to achieve compressive arch action (CAA) capacity. The strain and stress distribution at this state is shown in Figure 9.

$$15.\quad 0{\cdot}7N_b = C_s + C_c - T = f'_{scr}A'_s + 0{\cdot}85f'_c b\beta c_N - f_y A_s$$

where $f'_{scr} = E_s\varepsilon'_{scr} = E_s(1 - a'_s/c_N)\varepsilon_{cu}$, A'_s is the compressive bar area, b is the beam width and β is the ratio of the equivalent rectangular stress block depth to the neutral-axis depth, as defined in ACI 318-05 (ACI, 2005).

The neutral-axis depth c_N from Equation 15 is used to calculate the ultimate compressive force of concrete ($C_c = 0{\cdot}85f'_c b\beta c_N$). Before the strain of compression bars reaches ε'_{scr} (corresponding to concrete attaining ε_{cu}), C_c is linearly linked to the compression bar strain ε'_s. Therefore, the compressive spring force F_c is given by

$$16.\quad F_c = C_s + C_c = f'_s A'_s + (\varepsilon'_s/\varepsilon'_{scr})0{\cdot}85f'_c b\beta c_N$$

When ε'_s exceeds ε'_{scr}, C_c in Equation 16 is constant as $0{\cdot}85f'_c b\beta c_N$. The constitutive model of compression reinforcement is bilinear, the same as that of tension reinforcement. Therefore, F_c is a function of ε'_s.

As concrete excels at sustaining compression, the free end slip of compressive bars can be ignored and the loaded end slip solely depends on the bar contraction. The compressive elastic (τ_{EC}) and inelastic (τ_{YC}) bond strengths are taken as $2{\cdot}2(f'_c)^{0{\cdot}5}$ and $3{\cdot}6(f'_c)^{0{\cdot}5}$ respectively (Lowes and Altoontash, 2003). Similar to the derivation for tensile springs, the compressive bar stress–slip relationship is obtained by simply replacing τ_{ET} and τ_{YT} with τ_{EC} and τ_{YC} respectively, and is then converted to the force–slip relationship using Equation 16. Note that concrete is unable to follow compression reinforcement to a large strain. Moreover, compressive springs change into tensile springs when catenary action kicks in, and eventually fail in tension. Therefore, for compressive springs, the ultimate force is not a critical parameter, and a strain of $10\varepsilon_{cu}$ is tentatively used to determine the ultimate force and deformation. Finally, it is natural to locate the compressive spring at the centroid of compression reinforcement due to the transition of compression to tension (contributed by C_s only) in the loading history.

According to Equation 16, F_{c1} and F_{c2} denote the smaller and the

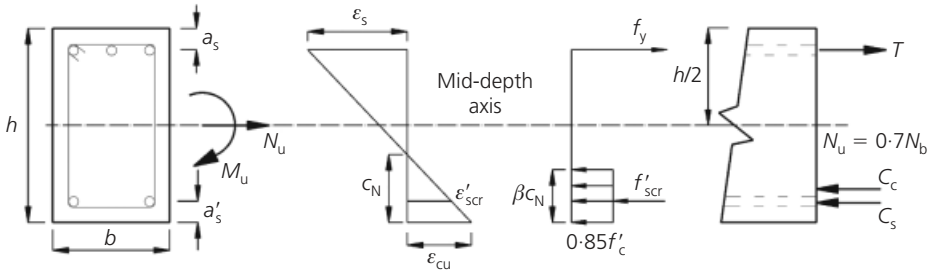

Figure 9. Stress and strain distribution at beam sections

larger capacity corresponding to concrete attaining a crushing strain ε_{cu} and compression reinforcement reaching the yield strain respectively, as shown in Figure 7. F_{c3} is the capacity at the strain of $10\varepsilon_{cu}$.

Validation of component-based joint model

Overall modelling parameters

The joint model is validated by comparisons of simulated and observed responses for RC assemblages S3, S4, S5 and S6 under a MCRS (Yu and Tan, 2013b). Each specimen consisted of one middle joint, two single-bay beams and two ECSs, as shown in Figure 1. The four specimens had the same dimensions but different reinforcement detailing. The span of each single-bay beam was 2750 mm. The cross-section was 250 mm depth by 150 mm width for beams, 250 mm square for the middle column and 400 mm by 450 mm for the ECSs. The top and bottom reinforcements in the joint and ECS interfaces of S4 were 3∅13 mm and 2∅13 mm respectively. In comparison to S4, the corresponding bottom reinforcement in S3 was changed to 2∅10 mm, the bottom one in S5 to 3∅13 mm, and the top one in S6 to 3∅16 mm. For all four specimens, one top bar was cut off at 1000 mm away from the middle joint and ECS interfaces. Stirrups with two legs of ∅6 mm were uniformly distributed throughout the beams with a spacing of 100 mm. For more information on specimen detailing, the reader is referred to the work of Yu and Tan (2013b). The compressive strength of concrete was 38·2 MPa and the material properties of the steel reinforcements are shown in Table 2. In calibrating the bar force–slip springs, the hardening modulus E_h was 1032, 929 and 753 MPa for ∅10, ∅13 and ∅16 mm respectively.

The joint model was incorporated into macro-FEA using Engineer's Studio software (Forum8, 2008), as shown in Figure 10. The beams near the joint and ECS interfaces were modelled with second-order fibre elements and the rest of beams with first-order fibre elements. Two ECSs were modelled with elastic beam elements. Besides the middle joint, the ECS interfaces were also modelled with an assembly of spring elements. Non-linear static analysis was conducted by applying a displacement at the top of the middle joint until the specimen failed.

Bar diameter: mm	Yield strength f_y: MPa	Elastic modulus E_s: MPa	Tensile strength f_u: MPa	Ultimate strain ε_u: %
6	349	199 177	459	—
10	511	211 020	622	11·00
13	494	185 873	593	10·92
16	513	184 423	612	13·43

Table 2. Material properties of steel reinforcement

The constitutive models for concrete and reinforcement developed by Maekawa *et al.* (2003), namely COM3, are were employed for the beams. The compressive branch of the concrete model was an elasto-plastic fracture model. As the beam had large cracks near the joint interfaces (Yu and Tan, 2013b), the confinement effect from stirrups was not considered. In COM3 models, the concrete between cracks can contribute tension due to bond, and average tensile stress–strain relationships are used for both concrete and steel reinforcement with an assumption of 'perfect bond'. After the tensile strength, concrete has a descending tensile branch. The average tensile yield stress of reinforcing bars depends on the effective reinforcement ratio. For bars in compression, buckling was not considered.

Similar to the tests, the top middle node in the joint was rotationally restrained. The horizontal restraints (namely, Top-RW, Btm-RW, Top-AF and Btm-AF, as indicated in Figure 10) were modelled using linear spring elements accounting for connection

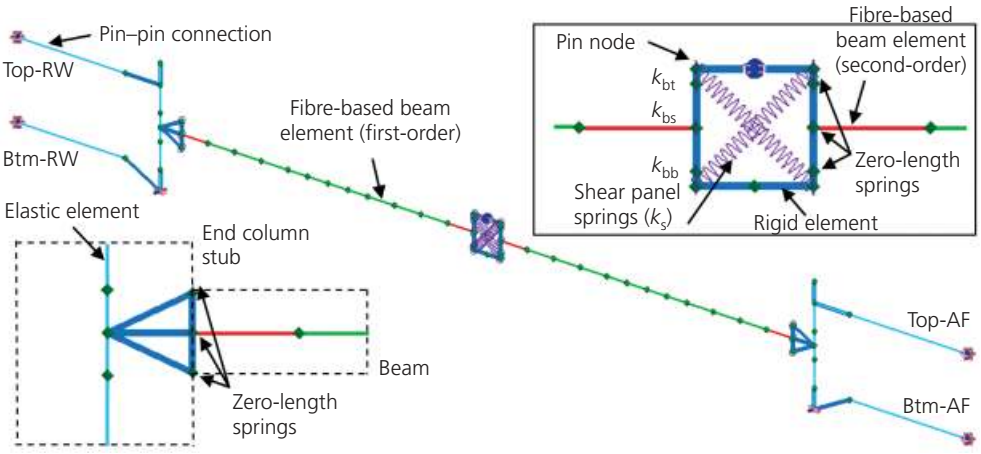

Figure 10. Macro finite-element model of assemblages

gaps. During the tests, the reaction force and the displacement of each restraint were measured. For simplicity, only the restraints of specimens S4 and S6 are shown in Figures 11(a) and 11(b) respectively. Each branch was used to evaluate the restraint stiffness and connection gaps by way of linear regression. Table 3 shows the restraint stiffnesses and gaps of specimens S4 and S6.

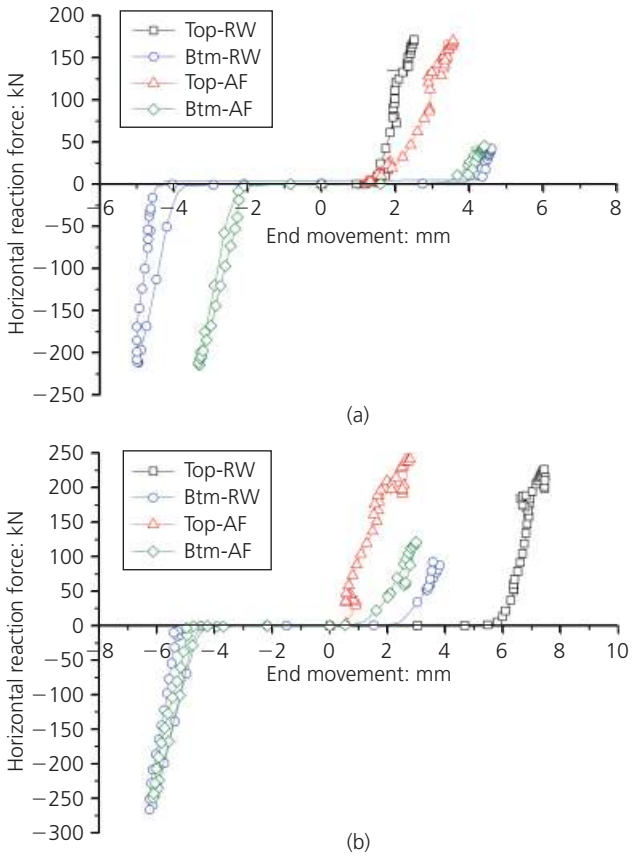

Figure 11. Stiffness of axial restraints at ECSs: (a) specimen S4; (b) specimen S6

Horizontal restraint	Tension stiffness: kN/m	Compression stiffness: kN/m	Tension gap: mm	Compression gap: mm
Specimen S4				
Top-RW	160 393	—	1·4	—
Btm-RW	82 650	254 495	4·1	−4·3
Top-AF	100 572	—	1·8	—
Btm-AF	49 255	175 277	3·5	−2·1
Specimen S6				
Top-RW	142 144	—	5·8	—
Btm-RW	67 813	204 322	2·5	−5·0
Top-AF	90 794	—	0·0	—
Btm-AF	80 139	175 093	1·5	−4·8

Table 3. Restraint stiffnesses and gaps

Spring parameters in component-based joints

The interface springs k_{bt}, k_{bs} and k_{bb} were modelled with zero-length springs, as indicated in the inset of Figure 10. The envelopes of the shear panel springs k_s and the bar force–slip springs k_{bb} and k_{bt} are shown in Figure 3(b) and Figure 7 respectively. In Engineer's Studio, unloading and reloading of springs are implemented using the Takeda hysteresis model. Because the material and geometric properties of the middle joints in the tests (Yu and Tan, 2013b) were nearly the same, the critical points of k_s were selected to be the same for all the specimens.

Without considering bond deterioration, the upper limit of the inelastic bond strength τ_{YT} was around $0{\cdot}25(f'_c)^{0{\cdot}5}$ using the bilinear reinforcement constitutive model (Yu and Tan, 2012). However, previous experiments showed that the bond deterioration zone could extend several times the bar diameter under a pullout force (Qureshi and Maekawa, 1993; Viawanthanatepa *et al.*, 1979). Thus, the bond deterioration more severely reduces τ_{YT} for bars with short embedment lengths. The bottom bars in the middle joints of S3 and S6 were lap-spliced, whereas those in S4 and S5 were continuous. With calibration on the anchored bars in S3 and S4, according to the embedment length and bond deterioration, τ_{YT} takes on values of $0{\cdot}1(f'_c)^{0{\cdot}5}$ and $0{\cdot}15(f'_c)^{0{\cdot}5}$ for the continuous and lap-spliced bars in the middle joints respectively, and $0{\cdot}2(f'_c)^{0{\cdot}5}$ for the anchored bars in the ECS.

The properties of springs k_{bt} and k_{bb} of specimens S4, S5 and S6 are shown in Tables 4 and 5. Spring k_{bb} at the middle joint interfaces (Table 4) and spring k_{bt} at the ECS interfaces (Table 5) transfer tension only. Note that the bar between two adjacent flexural cracks near a joint interface is under axial tension, and half the bar extension contributes to the ultimate slip of k_{bb} and k_{bt}. This contribution is more obvious when the embedment length in the joint is short. The beam bar extension is calculated in the same way as that for the continuous bar in the joint. For example, the ultimate slip of the bar embedded in the middle

	Spring k_{bt}						Spring k_{bb}			
	l_{embd}: mm	E_h: MPa	Tensile branch		Compressive branch		l_{embd}: mm	E_h: MPa	Tensile branch	
			S_t: mm	F_t: kN	S_c: mm	F_c: kN			S_t: mm	F_t: kN
S4	125 + (50)	929	0·30	196·71	0·068	477·52	125 + (50)	929	0·30	131·14
			7·93	216·42	0·157	544·63			7·93	144·28
			17·26	236·13	0·217	554·74			17·26	157·42
S5	125 + (25)	929	0·25	196·71	0·072	497·24	125 + (25)	929	0·25	196·71
			7·42	216·42	0·157	560·36			7·42	216·42
			16·75	236·13	0·217	570·47			16·75	236·13
S6	265	832	0·26	309·43	0·080	531·69	530	929	0·19	131·14
			9·98	339·29	0·210	649·57			5·28	144·28
			25·75	369·15	0·270	661·93			19·61	157·42

Table 4. Properties of springs k_{bb} and k_{bt} at middle joint interfaces. For S4 and S5, tensile slip includes extension of the beam bar near joint interfaces with the length indicated in brackets. However, for compressive slip, the contribution of beam bars is ignored

	Spring k_{bb}						Spring k_{bt}			
	l_{embd}: mm	E_h: MPa	Tensile branch		Compressive branch		l_{embd}: mm	E_h: MPa	Tensile branch	
			S_t: mm	F_t: kN	S_c: mm	F_c: kN			S_t: mm	F_t: kN
S4	425	929	0·19	131·14	0·074	461·35	425	929	0·19	196·71
			4·00	144·28	0·157	502·24			4·00	216·42
			14·75	157·42	0·216	508·98			14·75	236·13
S5	425 + (25)	929	0·25	196·71	0·072	497·25	425 + (25)	929	0·25	196·71
			5·34	216·42	0·157	560·36			5·34	216·42
			17·42	236·13	0·216	570·48			17·42	236·13
S6	425	929	0·19	131·14	0·070	481·49	425	832	0·26	309·43
			4·00	144·28	0·157	524·85			5·47	339·29
			14·75	157·42	0·216	531·59			20·21	369·15

Table 5. Properties of springs k_{bb} and k_{bt} at ECS interfaces. Specimen S5 includes the contribution of beam bar extension to total tensile slip

joint of S4 is around 12 mm. The spacing of severe flexural cracks is 100 mm, as shown in Figure 12, and the extension of the 50 mm long bar contributes about 5 mm to the slip of k_{bb}. Therefore, springs k_{bb} and k_{bt} at the middle joint interfaces of S4 and S5 include the contribution of beam bar extension, as indicated in Table 4. In addition, the top bars of S5 fractured at 50 mm away from the ECS interface, so the corresponding beam bar extension is considered. However, if the spacing of flexural cracks is not available in design, it can be estimated as one-half the maximum crack spacing computed according to Eurocode 2 (CEN, 2004). Without considering the slip from beam bar extension, the numerical simulations always predict bar fracture at a smaller middle joint displacement (MJD).

Comparison with experimental results

Figure 13 shows that the simulated structural behaviour of RC assemblages agrees well with the experimental results in terms of applied load–MJD and beam axial force–MJD relationships. This indicates that macro-FEA with the modified component-based joint model and the proposed calibration procedure on spring properties can represent essential structural behaviour (including CAA and catenary action) with satisfactory accuracy. Moreover,

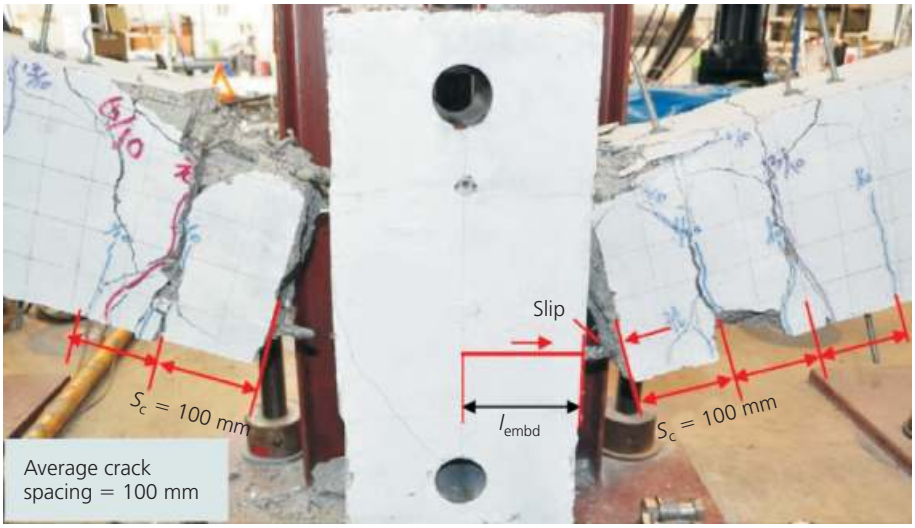

Figure 12. Contribution of beam bars to slip at joint interfaces of S4

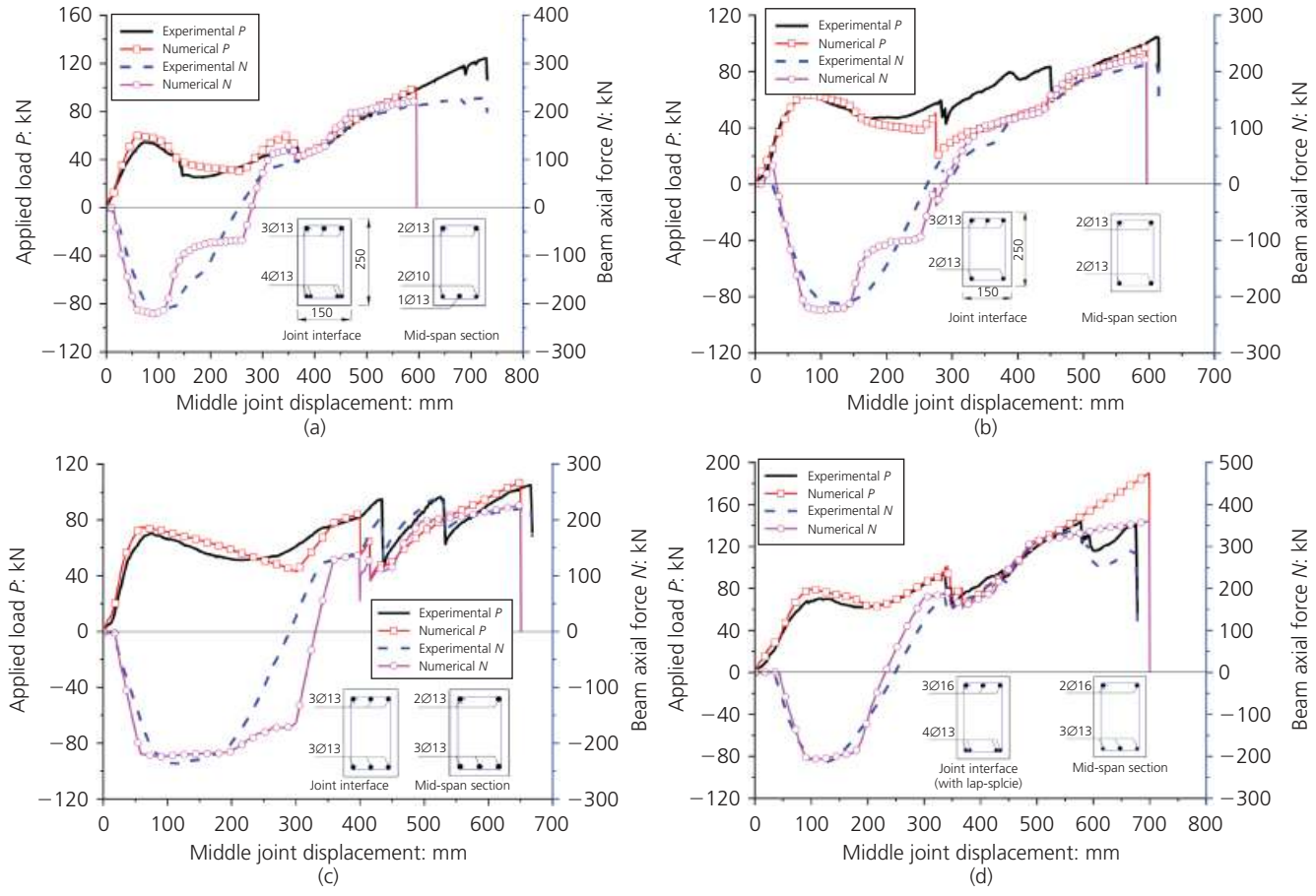

Figure 13. Validation of the proposed component-based joint model using macro-FEA: (a) specimen S3; (b)specimen S4; (c) specimen S5; (d) specimen S6

the effect of bar fracture on structural performance is predicted. Similar to the experimental results, the first fracture in numerical analyses occurred at spring k_{bb} of one middle joint interface and the final fracture at spring k_{bt} of one ECS interface. During the tests, the bottom bars at the joint interfaces sequentially fractured due to non-uniform material properties and imperfect construction. However, in the numerical analyses, springs k_{bb} at both joint interfaces fractured almost simultaneously. At the middle joint interfaces, after the fracture of k_{bb}, the beam axial force is transferred by k_{bt}. The good agreement between the numerical and experimental results in this range as shown in Figure 13 suggests that the proposed bar stress–slip model can provide appropriate tensile spring properties.

Discussion on numerical modelling schemes

To improve computational efficiency and simplify numerical modelling, another two modelling schemes are now discussed.

- Model 2 uses fibre beam elements and rigid joint models to save the procedure calibrating components in the joint model.
- Model 3 employs component-based joint models and fibre beam elements only for highly non-linear parts (including the plastic hinge zones near the joint interfaces and the both sides of a bar cut-off point), and elastic beam elements for the rest of the beam, as shown in Figure 14.

For simplicity, specimen S4 is used to demonstrate the effects of these two numerical modelling schemes, but the simulations on other specimens provided similar conclusions.

Figure 15(a) shows that model 2 overestimates CAA capacity and predicts early bar fracture. Model 2 also predicts early onset of catenary action when the beam axial force transfers from compression to tension, as shown in Figure 15(b). Under a MCRS, local rotation at the beam ends is contributed by both flexural and fixed-end rotations, in which the latter is attributed to bar slip at the joint interfaces. If joints are assumed rigid, as in model 2, the fixed-end rotation cannot be considered. Therefore, the assemblage presents a stiffer performance and bar fracture occurs with a smaller rotation of the beams and a smaller MJD of the assemblage.

Model 3 predicts almost the same results as model 1, as shown in Figure 15, indicating that model 3 is computationally efficient to simulate the structural behaviour of RC assemblages subjected to large deformations and severe discontinuity. Therefore, the numerical approach in model 3 is a feasible alternative to the extensive three-dimensional (3D) continuum-based FEA.

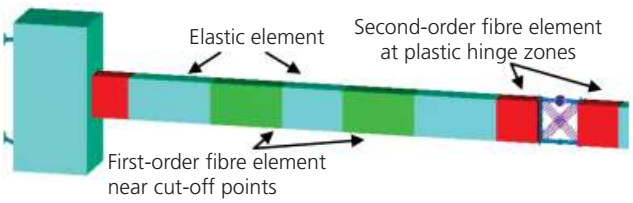

Figure 14. Numerical modelling with combination of elastic and fibre elements for beams

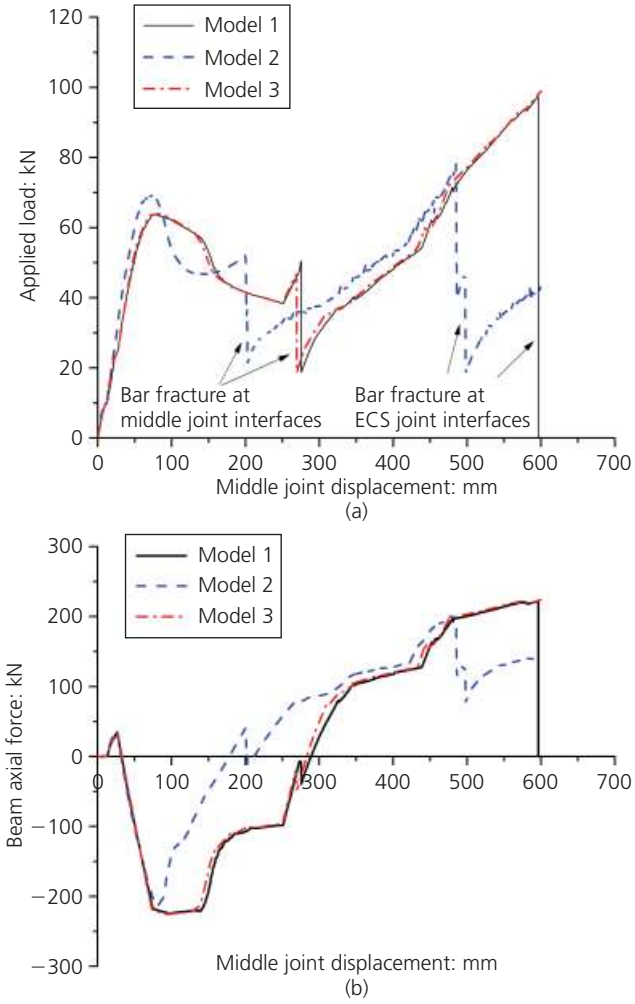

Figure 15. Effects of modelling schemes on load–deflection history: (a) applied load–MJD; (b) axial force–MJD. Model 1, fibre beam elements and component-based joint model; model 2, fibre beam elements and rigid joint model; model 3, combination of elastic and fibre beam elements and component-based joint model

Parametric study on structural behaviour of RC assemblages under a MCRS

Effect of imperfect boundaries

Specimen S4 was selected to illustrate the effects of boundary conditions (BCs) on the assemblage behaviour. The BCs of S4 contained restraint gaps, as shown in Figure 11(a). However, no gaps exist between structural members of monolithic RC

buildings. Therefore, to find out the effects of restraint gaps, a case study (i.e. case 2) with the same restraints at the ECS as S4 but with zero gaps is analysed.

In a 3D building, the BCs of the two-bay beam depend on the locations of the removed columns. For example, Figure 16(a) shows column removal scenarios for a typical office building with six spans by four bays. Due to symmetry, only half of the plan view is demonstrated. Except for the corner column removal scenario, the general BCs of the two-bay beam are shown in Figure 16(b). The in-plane restraints from the adjacent structural members can be simplified as vertical supports, lateral (K_a) and rotational (K_r) springs. Except for the corner and penultimate columns, the removal of any single column ensures the corresponding beams having adequate K_a (equivalent axial restraint stiffness) at least in one direction. Fully fixed ends (i.e. K_a and K_r tend to infinity) are the idealised BCs (i.e. case 3). For a penultimate column removal scenario (i.e. case 4), the idealised BCs are that one end is fully restrained and the other end is rotationally restrained but laterally unrestrained (Dat and Hai, 2013), say, $K_{a1} = 0$ and K_{r1} tends to infinity.

A comparison of cases 1 and 2 indicates that the presence of gaps reduces the stiffness and capacity at the CAA stage with beam axial compression, as shown in Figure 17. However, the gaps have little effect on catenary action. When the BCs are enhanced as fully fixed restraints in case 3, the CAA capacity increases by

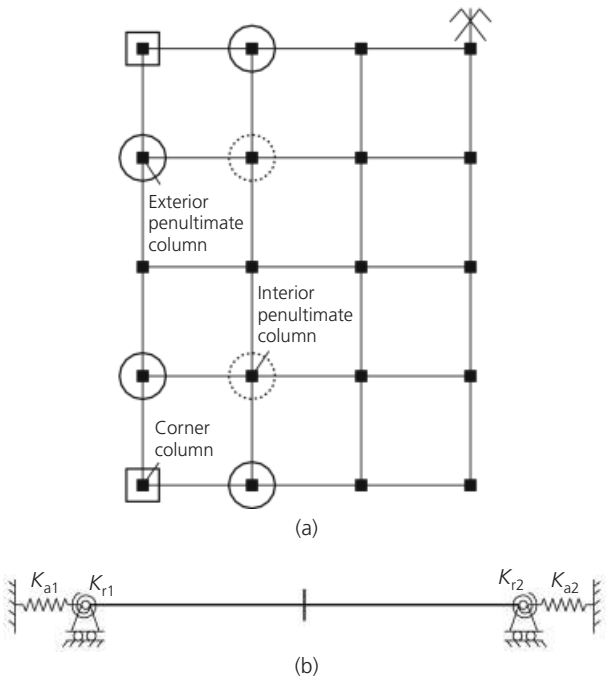

Figure 16. Boundary conditions of assemblages under different scenarios of column removal: (a) scenarios of column removal; (b) general boundary conditions of column removal scenario

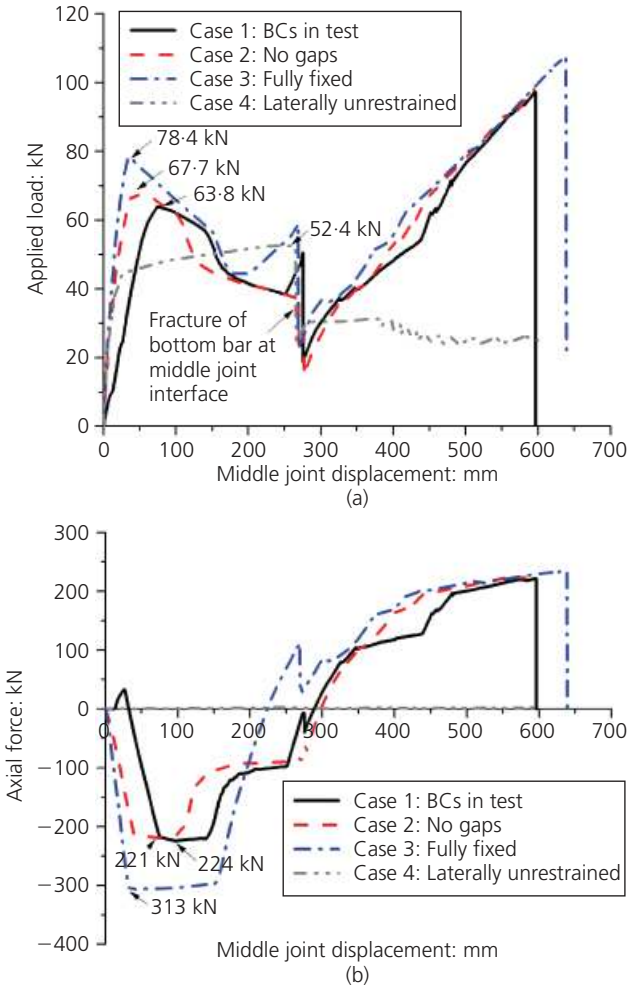

Figure 17. Effects of boundary conditions (BCs) on structural responses of RC assemblages: (a) load–MJD relationship; (b) axial force–MJD relationship

around 11% on top of case 2, and the maximum axial compression increases by around 41%, but the catenary action resistance has no evident improvement. When one beam end is laterally unrestrained (case 4), the beam axial force is not mobilised, as shown in Figure 17(b), indicating that the structural capacity is solely contributed by a flexural mechanism. Different from the other three cases, case 4 attains its maximum structural capacity of 52·4 kN at the fracture of bottom bars at one middle joint interface. Therefore, all measures to increase flexural resistance can be employed to mitigate the collapse potential caused by a penultimate column removal.

In summary, adequate lateral restraints must be provided to develop CAA and catenary action. Compared with catenary action, CAA is much more sensitive to imperfect restraint conditions, and a larger CAA capacity is achieved at stronger BCs.

Effect of bar curtailment

In RC structures, reinforcing bar curtailment is very common. Therefore, specimen S4 with fully fixed BCs (i.e. case 3 in Figure 17) is used here to investigate the effect of bar curtailment. In the first case, one top bar out of three is curtailed at 1000 mm away from the middle joint and ECS interfaces. In the second case, no curtailment is considered.

It is found that bar curtailment has an insignificant effect on the overall load–deflection relationships, suggesting that beam segments between the bar curtailment points can effectively transfer axial tension. However, bar curtailment causes the beam to deform in a more curved manner than one without curtailment at a large deflection (e.g. a MJD of 400–600 mm), as shown in Figure 18. The deformed shape at the left-hand side of Figure 18 indicates that, besides at the beam–column connections, an additional plastic hinge occurs near the bar curtailment point that faces the end support. Analyses on assemblages S5 and S6 came to the same findings.

Effect of beam depth

An assemblage with a beam depth less than its width was found to develop large catenary action capacity prior to bar fracture in tests (Sadek *et al.*, 2011). In addition, RC slabs can develop much greater resistances than yield line capacities by way of tensile membrane action (Park and Gamble, 2000), which is analogous to 'two-dimensional catenary action'. The above findings suggest that structural members with shallower sections are more suitable to develop catenary action. Therefore, the effect of beam depth on RC assemblage behaviour is considered here. Specimen S4 with fully fixed BCs at both ends (i.e. case 3) is chosen as the reference case. The other two cases have the same geometric and material properties as S4 except for beam cross-sectional dimensions. The beam section of S4 was 150 mm wide by 250 mm deep (150 × 250 for short). To maintain similar reinforcement ratios, beam sections of 190 × 200 and 250 × 150 were used for cases 5 and 6 respectively.

Figure 19(a) shows that a smaller beam depth results in a smaller CAA capacity, a larger catenary action resistance and a greater MJD at the first bar fracture at the middle joint interfaces. For example, case 6 with the shallowest beam depth (150 mm) reaches the smallest CAA capacity (28·0 kN) among the three cases, but attains the largest catenary action resistance (135·4 kN) at MJD = 572 mm at the first bar fracture. Figure 19(b) demonstrates that, with the same reinforcement, reducing the beam depth slightly decreases the maximum axial compression and causes the assemblage to transition into catenary action at a smaller MJD. However, the latter finding is not evident between cases 3 and 5.

Larger beam span-to-depth ratios result in smaller CAA capacity (Yu and Tan, 2014) and greater flexural rotation capacity (Panagiotakos and Fardis, 2001). That is, the global flexural behaviour is significantly affected by beam span-to-depth ratios. However, besides flexural deformation, fixed-end rotation at joint interfaces also contributes to assemblage deformation. The fixed-end rotation is mainly determined by the ultimate tensile slip at the joint interface and the distance of tension and compression reinforcement layers. When the tension reinforcement is less than the compression reinforcement at a beam section, the fixed-end rotation is more dominant. For instance, prior to imminent bar fracture, the fixed-end rotation at the middle joint interface of each case is much larger than that at the ECS interface, as shown in Table 6. The smaller fixed-end rotation is then used to calculate the lower bound of deflection due to slips. Table 6 demonstrates that fixed-end rotation contributes more than 49·5% of the total deflection in each case. Furthermore, with decreasing beam depth, the fixed-end rotations due to slip and the MJD at imminent bar fracture increase. Both unbroken beam reinforcement and large deflection help to develop catenary action resistance.

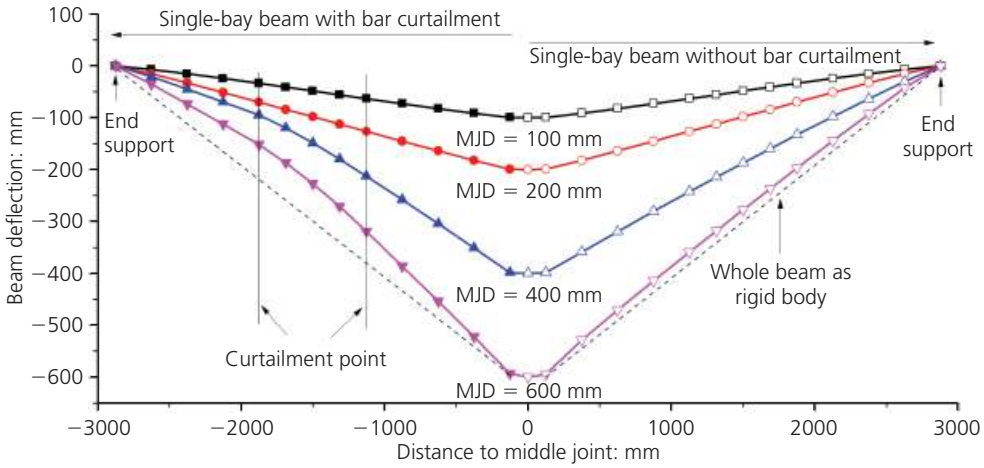

Figure 18. Effect of reinforcement curtailment on overall structural deformation of assemblages

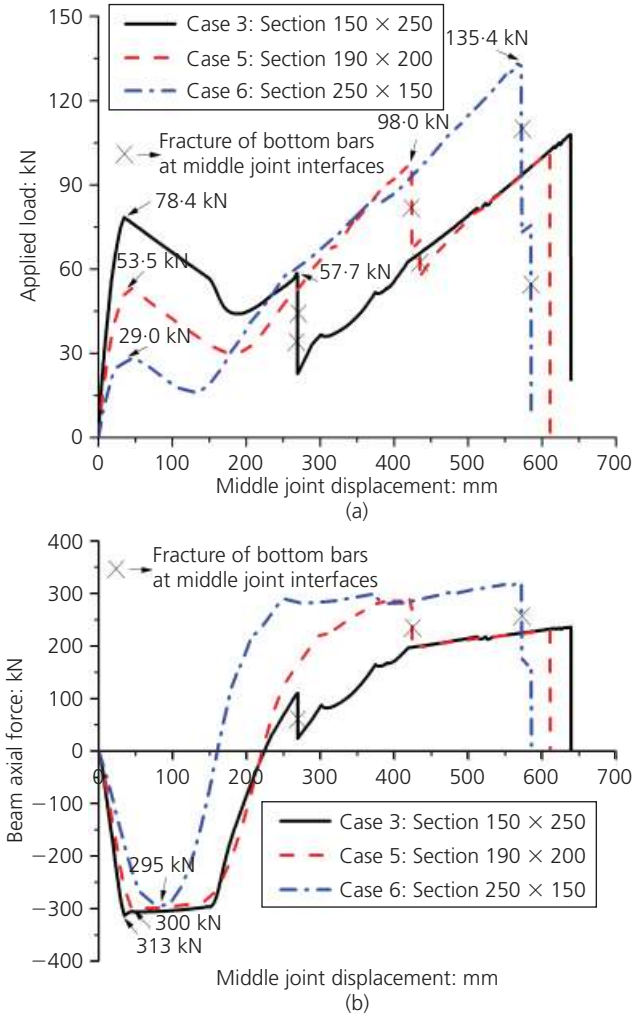

Figure 19. Effect of beam sections on structural responses of RC assemblages (section units: mm): (a) load–MJD relationship; (b) axial force–MJD relationship

Conclusions

A component-based joint model was modified to capture the effects of large slip and fracture of bars near joint interfaces on the structural behaviour of RC assemblages under a middle column removal scenario (MCRS). A systematic calibration procedure for each component was presented, in particular for the tensile bar force–slip spring, which governs the fixed-end rotation and bar fracture. Comparisons of numerical and experimental results indicate that macro-FEA with the joint model and fibre elements is able to characterise the essential structural mechanisms, including compressive arch action (CAA) and catenary action. Also, the modelling scheme of employing the joint models, fibre elements only for highly non-linear parts and elastic beam elements for the rest, was found to be more practical for simulating large-scale structures suffering progressive collapse.

With the joint model, catenary action resistance can be estimated properly. However, it is challenging to predict middle joint displacement at bar fracture with high precision. This is because the slip of post-yield bars depends on the inelastic bond strength, which is affected by the bar constitutive model, embedment length and bond deterioration. There is still a lack of adequate experimental data with which to calibrate this parameter. Following the presented calibration procedure, in particular ignoring the contribution of beam bar extension to the slips of interface springs, the prediction is conservative.

The numerical model was finally used to investigate the effects of boundary conditions, bar curtailment and beam depth on the structural behaviour of RC assemblages under a MCRS. The presence of connection gaps in restraints and finite restraint stiffnesses in the tests reduced the CAA capacity, but had no evident effect on catenary action. Moreover, due to the lack of adequate axial restraints to beams under a penultimate column removal scenario, CAA and catenary action are not mobilised and

Beam section: mm	MJD at bar fracture: mm	Fixed-end rotation: rad		Lower bound of deflection due to slip	
		At middle joint interface	At support interface	Corresponding MJD: mm[a]	Proportion of total deflection: %
(I)	(II)	(III)	(IV)	(V) = 2750 × min[(III), (IV)]	(VI) = (V)/(II)
150 × 250	259	0·0929	0·0484	133	49·5
190 × 200	423	0·1251	0·0925	254	60·1
250 × 150	585	0·1970	0·1375	378	64·6

[a] Deflection due to slip equals the net span (2750 mm in case studies) multiplied by fixed-end rotation.

Table 6. Deflection due to bar slip at the first imminent bar fracture from analysis

the two-bay beam has to rely on flexural capacity. Bar curtailment has an insignificant effect on the overall load–deflection history, but does affect the deformed configuration of beams at the catenary action stage. With the same parameters except for beam cross-sections, reducing the beam depth decreased CAA capacity, but significantly improved catenary action resistance at the first bar fracture through effectively converting bar slip into fixed-end rotation and increasing the flexural rotation capacity.

Acknowledgement

The authors gratefully acknowledge funding provided by the Defence Science & Technology Agency, Singapore.

REFERENCES

ACI (American Concrete Institute) (2005) ACI 318-05: Building code requirements for structural concrete. Farmington Hills, MI, USA.

Alsiwat JM and Saatcioglu M (1992) Reinforcement anchorage slip under monotonic loading. *Journal of Structural Engineering ASCE* **118(9)**: 2421–2438.

Bao YH, Kunnath SK, Ei-Tawil S and Lew HS (2008) Macromodel-based simulation of progressive collapse: RC frame structures. *Journal of Structural Engineering* **134(7)**: 1079–1091.

Bentz EC (2000) *Membrane-2000: Reinforced Concrete Membrane Analysis using the Modified Compression Field Theory*. University of Toronto, Toronto, ON, Canada.

CEN (Comité Européen de Normalisation) (2004) EN 1992-1-1: Eurocode 2: Design of concrete structures. Part 1.1: General rules and rules for buildings. CEN, Brussels, Belgium.

Cesare MA and Archilla JC (2006) A model for progressive collapse of conventional framed buildings. *Proceedings of Structures Congress 2006*. ASCE, Reston, VA, USA, pp. 1–16.

Dat PX and Hai TK (2013) Membrane actions of RC slabs in mitigating progressive collapse of building structures. *Engineering Structures* **55**: 107–115.

DoD (Department of Defense) (2010) *Unified Facilities Criteria (UFC) 4-023-03: Design of Buildings to Resist Progressive Collapse*. DoD, Arlington, VA, USA.

Dusenberry D and Hamburger R (2006) Practical means for energy-based analyses of disproportionate collapse potential. *Journal of Performance of Constructed Facilities* **20(4)**: 336–348.

Eligehausen R, Popov EP and Bertero VV (1983) *Local Bond Stress–Slip Relationships of Deformed Bars Under Generalized Excitations*. University of California, Berkeley, CA, USA, report UCB/EERC-83/23.

Filippou FC, Popov EP and Bertero VV (1983) *Effects of Bond Deterioration on Hysteretic Behavior of Reinforced Concrete Joints*. University of California, Berkeley, CA, USA, report UCB/EERC-83/19.

Forum8 (2008) *Engineer's Studio, 1.001*. See http://www.forum8.co.jp/english/uc-win/EngineersStudio-1e.htm (accessed 13/06/2014).

Grierson DE, Xu L and Liu Y (2005) Progressive-failure analysis of buildings subjected to abnormal loading. *Computer-Aided Civil and Infrastructure Engineering* **20(3)**: 155–171.

GSA (General Services of Administration) (2003) *Progressive Collapse Analysis and Design Guidelines for New Federal Office Buildings and Major Modernization Projects*. GSA, Washington, DC, USA.

Hansen E, Levine H, Lawver D and Tennant D (2006) Computational failure analysis of reinforced concrete structures subjected to blast loading. *Proceedings of Structures Congress 2006*. ASCE, Reston, VA, USA, pp. 1–13.

Izzuddin BA, Vlassis AG, Elghazouli AY and Nethercot DA (2008) Progressive collapse of multi-storey buildings due to sudden column loss – part 1: simplified assessment framework. *Engineering Structures* **30(8)**: 1308–1318.

Jaspart JP (2000) General report: session on connections. *Journal of Constructional Steel Research* **55(1–3)**: 69–89.

Lowes LN and Altoontash A (2003) Modeling reinforced-concrete beam–column joints subjected to cyclic loading. *Journal of Structural Engineering* **129(12)**: 1686–1697.

Luccioni BM, Ambrosini RD and Danesi RF (2004) Analysis of building collapse under blast loads. *Engineering Structures* **26(1)**: 63–71.

Maekawa K, Pimanmas A and Okamura H (2003) *Nonlinear Mechanics of Reinforced Concrete*. Spon, New York, USA.

Mitra N and Lowes LN (2007) Evaluation, calibration and verification of a reinforced concrete beam–column joint model. *Journal of Structural Engineering* **133(1)**: 106–120.

Panagiotakos TB and Fardis MN (2001) Deformation of reinforced concrete members at yielding and ultimate. *ACI Structural Journal* **98(2)**: 135–148.

Park R and Gamble WL (2000) *Reinforced Concrete Slabs*, 2nd edn. Wiley, Chichester, UK.

Qureshi J and Maekawa K (1993) Computational model for steel embedded in concrete under combined axial pullout and transverse shear displacement. *Proceedings of the Japan Concrete Institute* **15(2)**: 1249–1254.

Sadek F, Main JA, Lew HS and Bao Y (2011) Testing and analysis of steel and concrete beam–column assemblies under a column removal scenario. *Journal of Structural Engineering* **137(9)**: 881–892.

Su Y, Tian Y and Song X (2009) Progressive collapse resistance of axially-restrained frame beams. *ACI Structural Journal* **106(5)**: 600–607.

Vecchio FJ and Collins MP (1986) The modified compression-field theory for reinforced concrete elements subjected to shear. *ACI Structural Journal* **83(22)**: 219–231.

Viawanthanatepa S, Popov EP and Bertero VV (1979) *Effects of Generalized Loadings on Bond of Reinforcing Bars Embedded in Confined Concrete Blocks*. University of California, Berkeley, CA, USA, report UCB/EERC-79/22.

Yi WJ, He QF, Xiao Y and Kunnath SK (2008) Experimental study on progressive collapse-resistant behavior of reinforced concrete frame structures. *ACI Structural Journal* **105(4)**: 433–439.

Youssef M and Ghobarah A (2001) Modeling of RC beam–column joints and structural walls. *Journal of Earthquake Engineering* **5(1)**: 93–111.

Yu J (2012) *Structural Behavior of Reinforced Concrete Frames Subjected to Progressive Collapse*. PhD thesis, Nanyang Technological University, Singapore.

Yu J and Tan KH (2012) Bar stress–slip relationship in reinforced concrete joints with large inelastic bar strains. *Proceedings of 4th International Conference of Design and Analysis of Protective Structures, Jeju, Korea*, Paper #T9-5.

Yu J and Tan KH (2013a) Experimental and numerical investigation on progressive collapse resistance of reinforced concrete beam column sub-assemblages. *Engineering Structures* **55**: 90–106.

Yu J and Tan KH (2013b) Structural behavior of reinforced concrete beam–column sub-assemblages under a middle column removal scenario. *Journal of Structural Engineering* **139(2)**: 233–250.

Yu J and Tan KH (2014) Analytical model for the capacity of compressive arch action of reinforced concrete sub-assemblages. *Magazine of Concrete Research* **66(3)**: 109–126.